
STOCHASTIC MULTIGRID METHOD FOR BLIND PTYCHOGRAPHIC PHASE RETRIEVAL

A PREPRINT

 **Borong Zhang***
 Department of Mathematics
 University of Wisconsin, Madison
 Madison, WI 53706
 bzhang388@wisc.edu

 **Junjing Deng**
 Advanced Photon Science
 Argonne National Laboratory
 Lemont, IL 60439

 **Yi Jiang**
 Advanced Photon Science
 Argonne National Laboratory
 Lemont, IL 60439

 **Zichao Wendy Di**
 Mathematics and Computer Science & Advanced Photon Science
 Argonne National Laboratory
 Lemont, IL 60439

November 4, 2025

ABSTRACT

We present eMAGPIE (extended Multilevel–Adaptive–Guided Ptychographic Iterative Engine), a stochastic multigrid method for blind ptychographic phase retrieval that jointly recovers the object and the probe. We recast the task as the iterative minimization of a quadratic surrogate that majorizes the exit-wave misfit. From this surrogate, we derive closed-form updates, combined in a geometric-mean, phase-aligned joint step, yielding a simultaneous update of the object and probe with guaranteed descent of the sampled surrogate. This formulation naturally admits a multigrid acceleration that speeds up convergence. In experiments, eMAGPIE attains lower data misfit and phase error at comparable compute budgets and produces smoother, artifact-reduced phase reconstructions.

Keywords phase retrieval · multigrid optimization · inverse problems · ptychography · coherent diffraction imaging

1 Introduction

Ptychography is a coherent diffractive imaging technique that reconstructs high-resolution, complex-valued images from a series of diffraction patterns. It has had a broad impact in materials science [1], biological imaging [2, 3], and integrated-circuit metrology [4, 5] (see [6] for a survey). In a typical experiment, a coherent probe is scanned over overlapping regions of an object, and only the far-field intensities are measured, making the reconstruction a *phase-retrieval* problem.

Mathematically, ptychographic phase retrieval leads to a nonconvex and ill-posed inverse problem. A widely used class of solvers is the Ptychographical Iterative Engine (PIE) family [7, 8, 9], which casts reconstruction as an iterative sequence of data-consistent updates stabilized by quadratic regularization. In many practical settings, the probe is unknown, resulting in the *blind* problem in which both the object and the probe must be estimated jointly.

Ptychography naturally exhibits a multiscale character. Multigrid methods exploit this property by solving the problem across a hierarchy of discretizations [10]. In optimization, the MG/OPT framework extends these ideas to nonlinear objectives and constraints, often yielding substantial computational speedups [11]. Variants of MG/OPT have been developed and analyzed for a wide range of applications [12, 13, 14]. In inverse problems, multilevel hierarchies can further help mitigate ill-posedness by enforcing consistency across scales [15, 16, 17].

*Corresponding author.

In ptychography, coarsening the object and its associated exit-wave representations enables inexpensive global corrections before refining fine-scale details. Recent adaptations have demonstrated promising improvements [18]. In our prior work on the *non-blind* setting [19], we introduced MAGPIE (Multilevel–Adaptive–Guided Ptychographic Iterative Engine), a stochastic solver that (i) minimizes a majorizing quadratic surrogate of the exit-wave misfit and (ii) accelerates object updates through multigrid corrections. We also established a theoretical framework interpreting non-blind rPIE as a form of surrogate minimization [19].

In this work, we extend the surrogate-minimization framework to *blind* ptychography and introduce a joint object–probe update that minimizes the majorizing surrogate through simple per-pixel operations. A multigrid enhancement further accelerates convergence and improves stability. Our key contributions are as follows:

1. **Blind surrogate minimization.** We generalize the majorizing exit-wave surrogate of [19] to the blind setting, proving objective- and gradient-matching at the current iterate and establishing a global upper-bound (majorization) property that guarantees monotonic descent.
2. **Geometric-mean, phase-aligned joint update.** We derive a compact combination rule that fuses the individual minimizers for the object patch and probe via a geometric mean with phase alignment.
3. **Multilevel acceleration.** Consistent with [9], we find that, in typical optical regimes, reconstruction quality is far more sensitive to the object update than to the probe update; accordingly, we allocate more algorithmic effort to a stronger object step while using a standard, lightly tuned probe step, and we couple them via the proposed joint rule. For the object-patch subproblem, we employ MAGPIE, introduced in [19]. This yields faster, more stable convergence, particularly at low overlap ratios.
4. **Empirical validation.** Tests on simulated and experimental datasets show consistently lower reconstruction error, improved probe fidelity, and enhanced robustness to reduced overlap and elevated noise compared with current practice.

Organization. Section 2 formulates blind ptychography and notation and reviews PIE-family algorithms. Section 3 presents the blind majorizing surrogate, the joint update, and theoretical properties, and details the multilevel solver used for the object-patch subproblem and its interlevel operators/weights. Section 4 reports numerical results.

2 Preliminaries

2.1 2D blind ptychographic phase retrieval

In two-dimensional ptychographic phase retrieval, the goal is to reconstruct a complex-valued object $\mathbf{z}^* \in \mathbb{C}^{n^2}$ and probe $\mathbf{Q}^* \in \mathbb{C}^{m^2}$ (both vectorized) from overlapping far-field diffraction patterns. The data $\mathbf{d}_k \in \mathbb{R}^{m^2}$ are phaseless intensity measurements acquired at overlapping scan positions. Specifically,

$$\mathbf{d}_k = |\mathcal{F}(\mathbf{Q}^* \odot P_k \mathbf{z}^*)|^2 + \epsilon_k, \quad k = 1, \dots, N,$$

where N is the total number of scans, $P_k \in \{0, 1\}^{m^2 \times n^2}$ extracts the k th m^2 -pixel patch of the object (a binary selection/zero-padding operator), $\mathcal{F} \in \mathbb{C}^{m^2 \times m^2}$ denotes the two-dimensional discrete Fourier transform operator, $\epsilon_k \in \mathbb{R}^{m^2}$ corresponds to the noise associated with the k -th measurement, \odot denotes the Hadamard (element-wise) product, and $|\cdot|^2$ represents the element-wise intensity. The diagonal elements of P_k are 1 for the columns corresponding to the illuminated pixels in the k -th scanning region. We also refer to $\mathbf{Q}^* \odot P_k \mathbf{z}^*$ as the k -th exit wave. The overlap ratio refers to the fraction of the probe area that overlaps between adjacent scan positions. For example, a 50% overlap ratio means that the probe is shifted by half of its size in each direction when moving between neighboring positions. Higher overlap ratios increase data redundancy and generally improve the stability and convergence of reconstruction algorithms, at the cost of increased measurement acquisition [6]. Figure 1 illustrates the experimental setup and data acquisition process for ptychography.

Definition 2.1 (Revised Exit Wave). *For the k -th scanning region, define*

$$\mathbf{z}_k = P_k \mathbf{z},$$

and define the revised exit wave as

$$\mathcal{R}_k(\mathbf{Q}, \mathbf{z}_k) = \mathcal{F}^{-1} \left(\sqrt{\mathbf{d}_k} \odot \exp(i\theta(\mathcal{F}(\mathbf{Q} \odot \mathbf{z}_k))) \right),$$

where $\theta(\cdot)$ denotes the element-wise principal argument², and $\sqrt{\cdot}$ acts elementwise..

²Since $\theta(0)$ is undefined at index r , we set $[\theta(\mathcal{F}(\mathbf{Q} \odot \mathbf{z}_k))]_r = 0$ when $[\mathcal{F}(\mathbf{Q} \odot \mathbf{z}_k)]_r = 0$.

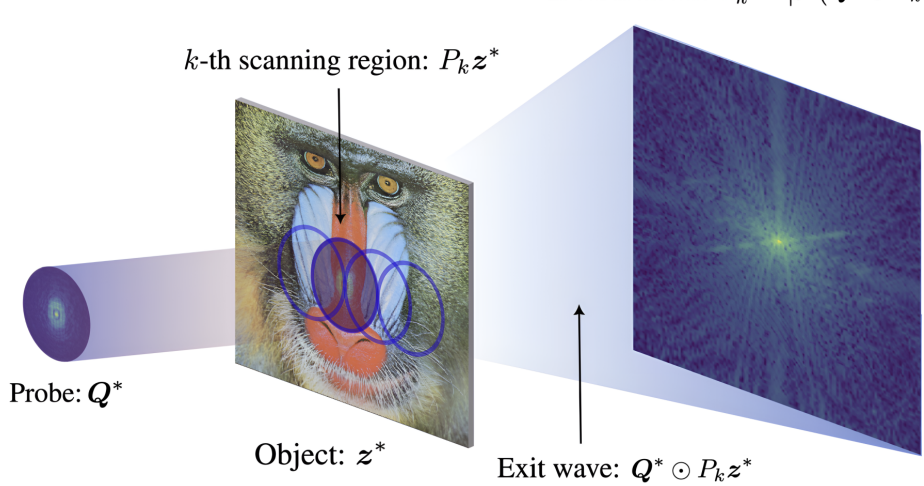


Figure 1: Experimental setup and data acquisition for ptychography.

The inverse problem is to infer \mathbf{z}^* and \mathbf{Q}^* from $\{d_k\}_{k=1}^N$, which is commonly formulated as minimizing the following misfit:

$$\begin{aligned} \min_{\mathbf{Q}, \mathbf{z}} \Phi(\mathbf{Q}, \mathbf{z}) &= \sum_{k=1}^N \Phi_k(\mathbf{Q}, \mathbf{z}_k), \\ &= \frac{1}{2} \sum_{k=1}^N \|\mathbf{Q} \odot P_k \mathbf{z} - \mathcal{R}_k(\mathbf{Q}, P_k \mathbf{z})\|_2^2. \end{aligned} \quad (1)$$

Since Φ is real-valued on complex variables, it is not complex-differentiable in the classical sense [20]. A common remedy is to employ the \mathbb{CR} -calculus [21]. To that end, we identify the complex vector $\mathbf{z}_k \in \mathbb{C}^{m^2}$ with its real and imaginary parts, writing $\mathbf{z}_k = \mathbf{x}_k + i\mathbf{y}_k$ and viewing it as an element of \mathbb{R}^{2m^2} . This lets us regard the objective as a mapping $\mathbb{R}^{2m^2} \rightarrow \mathbb{R}$. Under this identification, the complex gradient of Φ_k is

$$\begin{aligned} \nabla_{\mathbf{z}_k} \Phi_k &= \nabla_{\mathbf{x}_k} \Phi_k + i \nabla_{\mathbf{y}_k} \Phi_k \\ &= \overline{\mathbf{Q}} \odot (\mathbf{Q} \odot \mathbf{z}_k - \mathcal{R}_k(\mathbf{Q}, \mathbf{z}_k)). \end{aligned}$$

For a detailed computation, see [19]. Similarly, we have

$$\nabla_{\mathbf{Q}} \Phi_k = \overline{\mathbf{z}_k} \odot (\mathbf{Q} \odot \mathbf{z}_k - \mathcal{R}_k(\mathbf{Q}, \mathbf{z}_k)).$$

2.2 Ptychographic Iterative Engine (PIE)

The PIE family of algorithms [7, 8, 9] minimizes the exit-wave misfit in Eq. (1) via sequential, patchwise updates. In each iteration, the scan order is randomly permuted. For each selected scanning region k , we update the probe and the corresponding object patch by minimizing a regularized quadratic surrogate of Φ_k , while holding all entries outside that region fixed. One full sweep over all regions constitutes a single iteration.

Let $\mathbf{z}_k^{(j)}$ and $\mathbf{Q}^{(j)}$ denote the current estimates (object patch for region k and global probe) at iteration j . All products and fractions below are elementwise. The local rPIE update is

$$\begin{aligned} \mathbf{r}_k^{(j)} &:= \mathcal{R}_k \left(\mathbf{Q}^{(j)}, \mathbf{z}_k^{(j)} \right) - \mathbf{Q}^{(j)} \odot \mathbf{z}_k^{(j)}, \\ \mathbf{z}_k^{(j)} \leftarrow \mathbf{z}_k^+ &= \operatorname{argmin}_{\mathbf{z}_k} \tilde{\Phi}_k \left(\mathbf{Q}^{(j)}, \mathbf{z}_k; j \right) + \frac{1}{2} \left\langle \mathbf{u}_Q \left(\mathbf{Q}^{(j)} \right), \left| \mathbf{z}_k - \mathbf{z}_k^{(j)} \right|^2 \right\rangle, \\ &= \mathbf{z}_k^{(j)} + \frac{\overline{\mathbf{Q}^{(j)}}}{\mathbf{u}_Q \left(\mathbf{Q}^{(j)} \right) + \left| \mathbf{Q}^{(j)} \right|^2} \mathbf{r}_k^{(j)}, \\ \mathbf{Q}^{(j)} \leftarrow \mathbf{Q}^+ &= \operatorname{argmin}_{\mathbf{Q}} \tilde{\Phi}_k \left(\mathbf{Q}, \mathbf{z}_k^{(j)}; j \right) + \frac{1}{2} \left\langle \mathbf{u}_z \left(\mathbf{z}_k^{(j)} \right), \left| \mathbf{Q} - \mathbf{Q}^{(j)} \right|^2 \right\rangle, \\ &= \mathbf{Q}^{(j)} + \frac{\overline{\mathbf{z}_k^{(j)}}}{\mathbf{u}_z \left(\mathbf{z}_k^{(j)} \right) + \left| \mathbf{z}_k^{(j)} \right|^2} \mathbf{r}_k^{(j)}. \end{aligned} \tag{2}$$

Here \mathbf{u}_Q and \mathbf{u}_z are regularizers that control step sizes and stability. Within the PIE family, [9] reports the best performance for

$$\begin{aligned} \mathbf{u}_Q(\mathbf{Q}) &= \alpha_Q \left(\left\| \mathbf{Q} \right\|_\infty^2 - \left| \mathbf{Q} \right|^2 \right), \\ \mathbf{u}_z(\mathbf{z}) &= \alpha_z \left(\left\| \mathbf{z} \right\|_\infty^2 - \left| \mathbf{z} \right|^2 \right), \end{aligned}$$

with $\alpha_Q, \alpha_z > 0$ and $\left\| \cdot \right\|_\infty$ the entrywise sup norm (so $\left\| \mathbf{Q} \right\|_\infty^2 = \max_r |\mathbf{Q}_r|^2$). This scheme is the regularized Ptychographic Iterative Engine (rPIE).

Intuitively, where the probe illumination is weak ($|\mathbf{Q}_r| \ll 1$), the revised exit wave is more noise-sensitive, so the larger penalty \mathbf{u}_Q stabilizes the update; where illumination is strong, the penalty shrinks, reflecting higher measurement confidence. This adaptive weighting accelerates convergence and mitigates noise-induced instability.

3 Surrogate Minimization via a Multigrid Solver

In this section, we introduce a surrogate objective for Eqn. (1). This surrogate not only majorizes Eqn. (1) (see Section 3.1 for a precise definition of majorization) and iteratively recovers its optimal solution, but is also sufficiently general to encompass the entire PIE family of solvers. An equivalent formulation, presented in [22], has demonstrated superior performance on the general phase-retrieval problem.

Given the current solution $(\mathbf{Q}^{(j)}, \mathbf{z}^{(j)})$ at iteration j (e.g., from rPIE), we define the quadratic surrogate

$$\begin{aligned} \tilde{\Phi}(\mathbf{Q}, \mathbf{z}; j) &= \sum_{k=1}^N \tilde{\Phi}_k(\mathbf{Q}, \mathbf{z}_k; j), \\ &= \frac{1}{2} \sum_{k=1}^N \left\| \mathbf{Q} \odot \mathbf{z}_k - \mathcal{R}_k \left(\mathbf{Q}^{(j)}, \mathbf{z}_k^{(j)} \right) \right\|_2^2. \end{aligned} \tag{3}$$

When $\left[\mathcal{F} \left(\mathbf{Q}^{(j)} \odot \mathbf{z}_k^{(j)} \right) \right]_r = 0$ for some index r , we specify the phase as

$$\left[\theta \left(\mathcal{F} \left(\mathbf{Q}^{(j)} \odot \mathbf{z}_k^{(j)} \right) \right) \right]_r = \begin{cases} 0, & \text{if } j = 0 \text{ and } \left[\mathcal{F} \left(\mathbf{Q}^{(j)} \odot \mathbf{z}_k^{(j)} \right) \right]_r = 0, \\ \left[\theta \left(\mathcal{F} \left(\mathbf{Q}^{(j-1)} \odot \mathbf{z}_k^{(j-1)} \right) \right) \right]_r, & \text{if } j \geq 1 \text{ and } \left[\mathcal{F} \left(\mathbf{Q}^{(j)} \odot \mathbf{z}_k^{(j)} \right) \right]_r = 0, \\ \left[\theta \left(\mathcal{F} \left(\mathbf{Q}^{(j)} \odot \mathbf{z}_k^{(j)} \right) \right) \right]_r, & \text{otherwise.} \end{cases}$$

The next iteration solves

$$\left(\mathbf{Q}^{(j+1)}, \mathbf{z}^{(j+1)} \right) \in \operatorname{argmin}_{\mathbf{Q}, \mathbf{z}} \tilde{\Phi}(\mathbf{Q}, \mathbf{z}; j).$$

Because (3) is a sum over k , a stochastic strategy is natural: in each iteration, we randomly permute $\{1, \dots, N\}$ and update regions sequentially.³

$$(\tilde{\mathbf{Q}}, \tilde{\mathbf{z}}_k) \in \operatorname{argmin}_{\mathbf{Q}, \mathbf{z}_k} \tilde{\Phi}_k(\mathbf{Q}, \mathbf{z}_k; j), \quad \mathbf{Q}^{(j)} \leftarrow \tilde{\mathbf{Q}}, \mathbf{z}_k^{(j)} \leftarrow \tilde{\mathbf{z}}_k.$$

A common practice is to minimize the surrogate with respect to one variable while holding the other fixed, which recovers the rPIE updates in Eq. (2). However, the alternating pair $(\mathbf{Q}^+, \mathbf{z}_k^+)$ need not jointly minimize $\tilde{\Phi}_k$.

Additionally, a purely sequential update—first fixing \mathbf{Q} to update \mathbf{z}_k , then fixing the updated \mathbf{z}_k to update \mathbf{Q} —is ineffective: after the first step, the residual is already small, so the second step scarcely changes \mathbf{Q} . Instead, we update \mathbf{Q} and \mathbf{z}_k simultaneously as follows.

- Compute \mathbf{z}_k^+ by minimizing the surrogate with $\mathbf{Q}^{(j)}$ fixed:

$$\mathbf{z}_k^+ = \operatorname{argmin}_{\mathbf{z}_k} \tilde{\Phi}_k(\mathbf{Q}^{(j)}, \mathbf{z}_k; j). \quad (4)$$

- Compute \mathbf{Q}^+ by minimizing the surrogate with $\mathbf{z}_k^{(j)}$ fixed:

$$\mathbf{Q}^+ = \operatorname{argmin}_{\mathbf{Q}} \tilde{\Phi}_k(\mathbf{Q}, \mathbf{z}_k^{(j)}; j). \quad (5)$$

- Combine the one-variable minimizers via the geometric mean and phase alignment:

$$\begin{aligned} \tilde{\mathbf{z}}_k^2 &= \mathbf{z}_k^{(j)} \odot \mathbf{z}_k^+, \quad \left| \arg \left(\tilde{\mathbf{z}}_k \overline{\mathbf{z}_k^{(j)}} \right) \right| \leq \frac{\pi}{2}, \\ \tilde{\mathbf{Q}}^2 &= \mathbf{Q}^{(j)} \odot \mathbf{Q}^+, \quad \left| \arg \left(\tilde{\mathbf{Q}} \overline{\mathbf{Q}^{(j)}} \right) \right| \leq \frac{\pi}{2}. \end{aligned} \quad (6)$$

3.1 Properties of the Surrogate Minimization

The surrogate in Eq. (3) has several desirable properties and is consistent with the stochastic majorization–minimization (SMM) framework [23, 24, 25] (see Fig. 2).

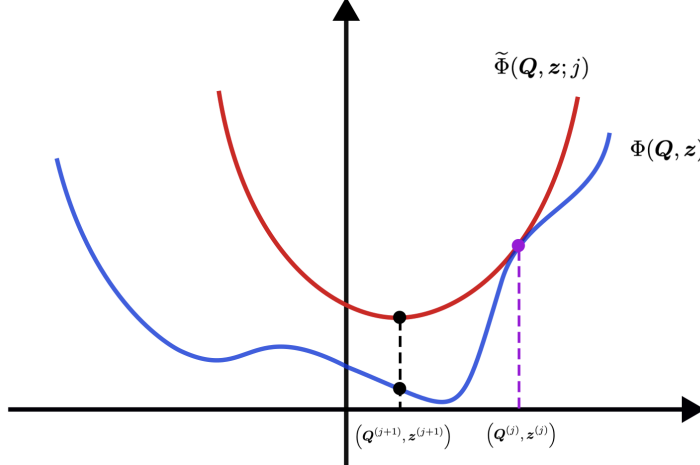


Figure 2: Illustration of the majorization property (adapted from [25]).

Proposition 3.1 (Majorization). *Let $\tilde{\Phi}(\mathbf{Q}, \mathbf{z}; j)$ be the surrogate in Eq. (3), and let $\Phi(\mathbf{Q}, \mathbf{z})$ be the exit-wave misfit in Eq. (1). Then:*

- *Objective agreement:*

$$\Phi(\mathbf{Q}^{(j)}, \mathbf{z}^{(j)}) = \tilde{\Phi}(\mathbf{Q}^{(j)}, \mathbf{z}^{(j)}; j).$$

³We increment j after all scanning positions have been visited.

- *Majorization: for all $\mathbf{Q} \in \mathbb{C}^{m^2}$ and $\mathbf{z} \in \mathbb{C}^{n^2}$,*

$$\Phi(\mathbf{Q}, \mathbf{z}) \leq \tilde{\Phi}(\mathbf{Q}, \mathbf{z}; j).$$

- *First-order agreement: for each k ,*

$$\nabla_{\mathbf{z}_k} \Phi_k \left(\mathbf{Q}^{(j)}, \mathbf{z}_k^{(j)} \right) = \nabla_{\mathbf{z}_k} \tilde{\Phi}_k \left(\mathbf{Q}^{(j)}, \mathbf{z}_k^{(j)}; j \right), \quad \nabla_{\mathbf{Q}} \Phi_k \left(\mathbf{Q}^{(j)}, \mathbf{z}_k^{(j)} \right) = \nabla_{\mathbf{Q}} \tilde{\Phi}_k \left(\mathbf{Q}^{(j)}, \mathbf{z}_k^{(j)}; j \right).$$

Proof. See [19]; a related argument appears in [22]. \square

With the majorization–minimization framework in place, we reduce the original optimization problem to the iterative minimization of simple quadratic surrogates.

To mitigate numerical instabilities caused by near-zero magnitudes in \mathbf{Q} or \mathbf{z}_k , we regularize the subproblems in Eqs. (4) and (5) and establish the descent property of the joint update—via a geometric-mean amplitude blend and phase alignment—in Proposition 3.2.

Proposition 3.2. *Suppose \mathbf{z}_k^+ and \mathbf{Q}^+ are obtained from the regularized surrogates:*

- *With $\mathbf{Q}^{(j)}$ fixed,*

$$\mathbf{z}_k^+ = \operatorname{argmin}_{\mathbf{z}_k} \tilde{\Phi}_k \left(\mathbf{Q}^{(j)}, \mathbf{z}_k; j \right) + \frac{1}{2} \left\langle \mathbf{u}_{\mathbf{Q}} \left(\mathbf{Q}^{(j)} \right), \left| \mathbf{z}_k - \mathbf{z}_k^{(j)} \right|^2 \right\rangle. \quad (7)$$

- *With $\mathbf{z}_k^{(j)}$ fixed,*

$$\mathbf{Q}^+ = \operatorname{argmin}_{\mathbf{Q}} \tilde{\Phi}_k \left(\mathbf{Q}, \mathbf{z}_k^{(j)}; j \right) + \frac{1}{2} \left\langle \mathbf{u}_{\mathbf{z}} \left(\mathbf{z}_k^{(j)} \right), \left| \mathbf{Q} - \mathbf{Q}^{(j)} \right|^2 \right\rangle. \quad (8)$$

- *Combine the one-variable minimizers via geometric averaging and phase alignment:*

$$\begin{aligned} \tilde{\mathbf{z}}_k^2 &= \mathbf{z}_k^{(j)} \odot \mathbf{z}_k^+, \quad \left| \arg \left(\tilde{\mathbf{z}}_k \mathbf{z}_k^{\overline{(j)}} \right) \right| \leq \frac{\pi}{2}, \\ \tilde{\mathbf{Q}}^2 &= \mathbf{Q}^{(j)} \odot \mathbf{Q}^+, \quad \left| \arg \left(\tilde{\mathbf{Q}} \mathbf{Q}^{\overline{(j)}} \right) \right| \leq \frac{\pi}{2}. \end{aligned}$$

Then

$$\tilde{\Phi}_k \left(\tilde{\mathbf{Q}}, \tilde{\mathbf{z}}_k; j \right) \leq \max \left\{ \tilde{\Phi}_k \left(\mathbf{Q}^+, \mathbf{z}_k^{(j)}; j \right), \tilde{\Phi}_k \left(\mathbf{Q}^{(j)}, \mathbf{z}_k^+; j \right) \right\} < \tilde{\Phi}_k \left(\mathbf{Q}^{(j)}, \mathbf{z}_k^{(j)}; j \right).$$

Proof. It suffices to argue entrywise. Fix an index r and set

$$\begin{aligned} q &= \mathbf{Q}_r^{(j)}, \quad z = \left(\mathbf{z}_k^{(j)} \right)_r, \quad d = \left[\mathcal{R}_k \left(\mathbf{Q}^{(j)}, \mathbf{z}_k^{(j)} \right) \right]_r, \quad u_z = \mathbf{u}_{\mathbf{z}} \left(\mathbf{z}_k^{(j)} \right)_r, \quad u_q = \mathbf{u}_{\mathbf{Q}} \left(\mathbf{Q}^{(j)} \right)_r, \\ q^+ &= \mathbf{Q}_r^+, \quad z^+ = (\mathbf{z}_k^+)_r, \quad \tilde{q} = \tilde{\mathbf{Q}}_r, \quad \tilde{z} = (\tilde{\mathbf{z}}_k)_r. \end{aligned}$$

From (7)–(8),

$$z^+ = z + \frac{\bar{q}}{|q|^2 + u_q} (d - qz), \quad q^+ = q + \frac{\bar{z}}{|z|^2 + u_z} (d - qz). \quad (9)$$

Let $e := qz - d$ and define

$$\alpha := \frac{u_q}{|q|^2 + u_q} \in (0, 1), \quad \beta := \frac{u_z}{|z|^2 + u_z} \in (0, 1).$$

Then (9) implies

$$X := qz^+ = d + \alpha e, \quad Y := q^+z = d + \beta e, \quad (10)$$

so $X - d$ and $Y - d$ are positive multiples of e (hence X and Y lie on the line through d with direction e).

By the geometric–mean construction,

$$\tilde{z}^2 = zz^+, \quad \tilde{q}^2 = qq^+, \quad |\arg(\tilde{z}) - \arg(z)| \leq \frac{\pi}{2}, \quad |\arg(\tilde{q}) - \arg(q)| \leq \frac{\pi}{2}.$$

Let $w := \tilde{q}\tilde{z}$. Then

$$w^2 = (\tilde{q}^2)(\tilde{z}^2) = (qq^+)(zz^+) = (qz^+)(q^+z) = XY.$$

and our branch choice yields

$$|\arg(w\bar{X})| \leq \frac{\pi}{2}, \quad \text{and} \quad |\arg(w\bar{Y})| \leq \frac{\pi}{2}. \quad (11)$$

Geometric lemma (Thales disk). Let $s, t \in \mathbb{C}$ with $s^2 = X, t^2 = Y$, and $st = w$. Then

$$(w - X)\overline{(w - Y)} = (st - s^2)(\overline{st - t^2}) = -s\bar{t}|s - t|^2,$$

so $\Re((w - X)\overline{(w - Y)}) \leq 0$ whenever $\Re(st) \geq 0$, which is equivalent to $|\arg(st)| \leq \frac{\pi}{2}$. Indeed, by Eqn. (11), we have

$$|\arg(st)| = \frac{1}{2}|\arg(ss\bar{t}t)| = \frac{1}{2}|\arg(X\bar{Y})| = \frac{1}{2}|\arg(X\bar{w}w\bar{Y})| \leq \frac{1}{2}(|\arg(X\bar{w})| + |\arg(w\bar{Y})|) \leq \frac{\pi}{2}.$$

Therefore, w lies in the closed disk with diameter $[X, Y]$.

Distance to a point on the diameter line. Because d lies on the line through X and Y (by (10)), a projection argument yields

$$|w - d| \leq \max\{|X - d|, |Y - d|\}.$$

Using (10), the right-hand side equals $\max\{\alpha|e|, \beta|e|\} = \max\{\alpha, \beta\}|qz - d|$. Thus

$$|\tilde{q}\tilde{z} - d| \leq \max\left\{\frac{u_q}{|q|^2 + u_q}, \frac{u_z}{|z|^2 + u_z}\right\}|qz - d| < |qz - d|,$$

with strict inequality whenever $e \neq 0$ and $u_q, u_z > 0$. Summing over r yields the claim. \square

The quadratic surrogate in (3) is tight and majorizes the exit-wave misfit. At each iteration, we sample a scan index k , build the corresponding regularized surrogate $\tilde{\Phi}_k(\mathbf{Q}, \mathbf{z}_k; j)$, compute its one-variable minimizers in closed form, and combine them via a geometric-mean amplitude rule with phase alignment to obtain an exact proximal update of $(\mathbf{Q}, \mathbf{z}_k)$. This update strictly decreases the sampled surrogate (cf. Proposition 3.2). For general theoretical background on stochastic majorization-minimization, see [23, 24, 25].

3.2 Extended MAGPIE (eMAGPIE)

The Multilevel-Adaptive-Guided Ptychographic Iterative Engine (MAGPIE) [19] accelerates the object-patch update by coupling a majorizing quadratic surrogate with a multigrid proximal scheme. For a fixed probe $\mathbf{Q}^{(j)}$, the fine-grid surrogate takes the form:

$$\begin{aligned} & \min_{\mathbf{z}_k} \tilde{\Phi}_k(\mathbf{Q}^{(j)}, \mathbf{z}_k; j) + \frac{1}{2} \left\langle \mathbf{u}_{\mathbf{Q}}(\mathbf{Q}^{(j)}), |\mathbf{z}_k - \mathbf{z}_k^{(j)}|^2 \right\rangle, \\ &= \frac{1}{2} \left\| \mathbf{Q}^{(j)} \odot \mathbf{z}_k - \mathcal{R}_k(\mathbf{Q}^{(j)}, \mathbf{z}_k^{(j)}) \right\|_2^2 + \frac{1}{2} \left\langle \mathbf{u}_{\mathbf{Q}}(\mathbf{Q}^{(j)}), |\mathbf{z}_k - \mathbf{z}_k^{(j)}|^2 \right\rangle. \end{aligned} \quad (12)$$

A corresponding coarse-grid surrogate is formed by restricting the terms in (12):

$$\begin{aligned} & \min_{\mathbf{z}_{H,k}} \tilde{\Phi}_{H,k}(\mathbf{Q}_H^{(j)}, \mathbf{z}_{H,k}; j) + \frac{1}{2} \left\langle \mathbf{u}_{H,\mathbf{Q}}(\mathbf{Q}^{(j)}), |\mathbf{z}_{H,k} - \mathbf{z}_{H,k}^{(j)}|^2 \right\rangle, \\ &= \frac{1}{2} \left\| \mathbf{Q}_H^{(j)} \odot \mathbf{z}_{H,k} - \mathcal{R}_{H,k}(\mathbf{Q}^{(j)}, \mathbf{z}_k^{(j)}) \right\|_2^2 + \frac{1}{2} \left\langle \mathbf{u}_{H,\mathbf{Q}}(\mathbf{Q}^{(j)}), |\mathbf{z}_{H,k} - \mathbf{z}_{H,k}^{(j)}|^2 \right\rangle. \end{aligned} \quad (13)$$

Specifically, we use weights

$$\mathbf{W}_{\mathbf{z}} = \frac{|\mathbf{Q}^{(j)}|^2}{\mathbf{I}_H^H \mathbf{I}_h^H |\mathbf{Q}^{(j)}|^2}, \quad \mathbf{W}_{\mathcal{R}} = \frac{(\mathbf{I}_H^H \mathbf{Q}_H^{(j)}) \odot \mathbf{W}_{\mathbf{z}}}{\mathbf{Q}^{(j)}}, \quad \mathbf{W}_{\mathbf{u}}^H = \frac{|\mathbf{Q}_H^{(j)}|^2}{\mathbf{I}_h^H |\mathbf{Q}^{(j)}|^2}, \quad (14)$$

where \mathbf{I}_h^H and $\mathbf{I}_H^H = 4(\mathbf{I}_h^H)^\top$ denote restriction and prolongation operators satisfying $\mathbf{I}_h^H \mathbf{I}_H^H = \mathbf{I}_{n_H^2}$, and we restrict the terms as

$$\begin{aligned} \mathbf{Q}_H^{(j)} &= \mathbf{I}_h^H \mathbf{Q}^{(j)}, \\ \mathbf{z}_{H,k}^{(j)} &= \mathbf{I}_h^H (\mathbf{W}_{\mathbf{z}} \odot \mathbf{z}_k^{(j)}), \\ \mathcal{R}_{H,k}(\mathbf{Q}^{(j)}, \mathbf{z}_k^{(j)}) &= \mathbf{I}_h^H (\mathbf{W}_{\mathcal{R}} \odot \mathcal{R}_k(\mathbf{Q}^{(j)}, \mathbf{z}_k^{(j)})), \\ \mathbf{u}_H(\mathbf{Q}^{(j)}) &= \mathbf{W}_{\mathbf{u}}^H \odot \mathbf{I}_h^H \mathbf{u}_{\mathbf{Q}}(\mathbf{Q}^{(j)}). \end{aligned} \quad (15)$$

Solving (12)–(13) in closed form yields

$$\begin{aligned}\hat{z}_{H,k}^{(j)} &= z_{H,k}^{(j)} + \frac{\overline{\mathbf{Q}_H^{(j)}}}{\mathbf{u}_H(\mathbf{Q}^{(j)}) + |\mathbf{Q}_H|} \odot \left(\mathcal{R}_{H,k}(\mathbf{Q}_H^{(j)}, z_{H,k}^{(j)}) - \mathbf{Q}_H^{(j)} \odot z_{H,k}^{(j)} \right), \\ z'_k &= z_k^{(j)} + \mathbf{I}_H^h \left(\hat{z}_{H,k}^{(j)} - z_{H,k}^{(j)} \right), \\ z_k^+ &= z'_k + \frac{\overline{\mathbf{Q}^{(j)}}}{\mathbf{u}(\mathbf{Q}^{(j)}) + |\mathbf{Q}^{(j)}|} \odot \left(\mathcal{R}_k(\mathbf{Q}^{(j)}, z_k^{(j)}) - \mathbf{Q}^{(j)} \odot z'_k \right).\end{aligned}$$

In [19], we established several desirable properties of MAGPIE:

- **Well-defined weights:** $\|\mathbf{W}_z\|_\infty \leq 4$, $\|\mathbf{W}_\mathcal{R}\|_\infty \leq 4$, and $\|\mathbf{W}_u\|_\infty \leq 1$ prevent blow-up when $|\mathbf{Q}^{(j)}|$ is small.

- **Consistency.** The coarse-grid surrogate and its gradient are consistent with their fine-grid counterparts:

$$\begin{aligned}\tilde{\Phi}_{H,k}(\mathbf{Q}_H^{(j)}, z_{H,k}; j) &\leq \frac{1}{4} \|\mathbf{W}_\mathcal{R}\|_\infty^2 \tilde{\Phi}_k(\mathbf{Q}^{(j)}, z_k; j), \\ \left\| \nabla_{z_{H,k}} \tilde{\Phi}_{H,k}(\mathbf{Q}_H^{(j)}, z_{H,k}; j) \right\|_2 &\leq \frac{1}{2} \|\mathbf{W}_u\|_\infty \left\| \nabla_{z_k} \tilde{\Phi}_k(\mathbf{Q}^{(j)}, z_k; j) \right\|_2.\end{aligned}$$

- **Descent.** The coarse proximal step (??) yields a coarse-to-fine direction $\mathbf{I}_H^h(\hat{z}_{H,k} - z_{H,k}^{(j)})$ that is a descent direction for $\tilde{\Phi}_k$ at $z_k^{(j)}$:

$$\nabla_{z_k} \tilde{\Phi}_k(\mathbf{Q}^{(j)}, z_k; j)^* \mathbf{I}_H^h(\hat{z}_{H,k} - z_{H,k}^{(j)}) \leq 0.$$

- **Automatic regularization transfer.** With $\mathbf{u}_H(\mathbf{Q}^{(j)})$ chosen as in Eq. (15), the stability of fine- and coarse-grid updates is matched without manual tuning.

Rigorous statements and proofs are given in [19].

We employ MAGPIE for the object update in Eqn. (4) and a geometric-mean, phase-aligned rule for the joint object–probe update in Eqn. (6); we call the resulting solver extended MAGPIE (eMAGPIE).

4 Numerical Examples

In this section, we present numerical examples to demonstrate the performance of eMAGPIE. We compare our solver with the classical method rPIE [9]. To ensure a fair comparison with rPIE, we adopt its regularization terms for the object-patch update as the fine-grid regularization for eMAGPIE, i.e.,

$$u_Q(\mathbf{Q}^{(j)}) = \alpha \left(\left\| \mathbf{Q}^{(j)} \right\|_\infty^2 - \left| \mathbf{Q}^{(j)} \right|^2 \right).$$

For both algorithms, we use the ePIE probe update:

$$u_z(z_k^{(j)}) = \left\| z_k^{(j)} \right\|_\infty^2 - \left| z_k^{(j)} \right|^2.$$

We observe that the computational bottleneck at each iteration stems from the Fourier transforms required to evaluate $\mathcal{R}_k(\mathbf{Q}^{(j)} z_k^{(j)})$. Since this term is computed only once per scanning region at each iteration, eMAGPIE and rPIE share comparable per-iteration computational costs.

We first describe the problem setup, and then in Sections 4.2 and 4.3, we evaluate the performance of the algorithms from two perspectives: the effect of the overlap ratio and robustness to noise. Finally, Section 4.4 evaluates the algorithms on real datasets.

4.1 Experiment Setup

Probe In our numerical experiments, we use a simulated Fresnel zone plate as the probe (see [26]). The standard probe size is $m = 128$. Figure 3 shows the probe’s magnitude and phase. The magnitude exhibits the characteristic circular structure of a zone plate, while the phase displays the corresponding alternating concentric patterns. Notably, much of the probe outside the central region has a very low magnitude, which can lead to ill-conditioning.

Object We test on a synthetic object that is constructed by combining two standard test images: the Baboon image for magnitude and the Cameraman image for phase. The Baboon image is normalized to $[0, 1]$ to represent magnitude, and the Cameraman image is scaled to $[0, \frac{\pi}{2}]$ to provide the phase distribution. The object is represented at a resolution of $n = 512$ and displayed in Figure 3.

Probe and object initialization

- **Synthetic probe.** We form the initial probe $\mathbf{Q}^{(0)}$ from the ground-truth probe \mathbf{Q}^* by (i) smoothing its magnitude with a Gaussian blur in the Fourier domain to remove fine structure and (ii) adding low-order phase aberrations. Concretely, we use a Gaussian blur with $\sigma_{\text{amp}} = 2$ pixels, a random linear phase ramp of total magnitude ≈ 7 rad across the field of view, and quadratic terms for defocus and astigmatism with coefficients 0.6 and 0.2, respectively; a small complex noise of 1% amplitude is also added. This yields

$$\mathbf{Q}^{(0)} = (\mathcal{G}_{\sigma_{\text{amp}}} |\mathbf{Q}^*|) \exp \{ i[a_x x + a_y y + 0.6(x^2 + y^2) + 0.2(x^2 - y^2)] \},$$

with (a_x, a_y) drawn uniformly to produce a ~ 7 rad ramp.

- **Normalization and object initialization.** In both cases, we scale the probe to a fixed ℓ_2 norm set by the measured diffraction data $\{\mathbf{d}_k\}_{k=1}^N$. Let $\bar{\mathbf{d}} = \frac{1}{N} \sum_{k=1}^N \mathbf{d}_k$ and let m be the probe side lengths (in pixels). We define

$$\text{dp_avg} = \frac{\sqrt{\sum_{i,j} \bar{d}_{ij}}}{m}, \quad \mathbf{Q}^{(0)} \leftarrow \mathbf{Q}^{(0)} \frac{\text{dp_avg}}{\|\mathbf{Q}^{(0)}\|_2}.$$

The object is initialized to a constant field, $\mathbf{z}^{(0)} \equiv 1$ (unit amplitude, zero phase).

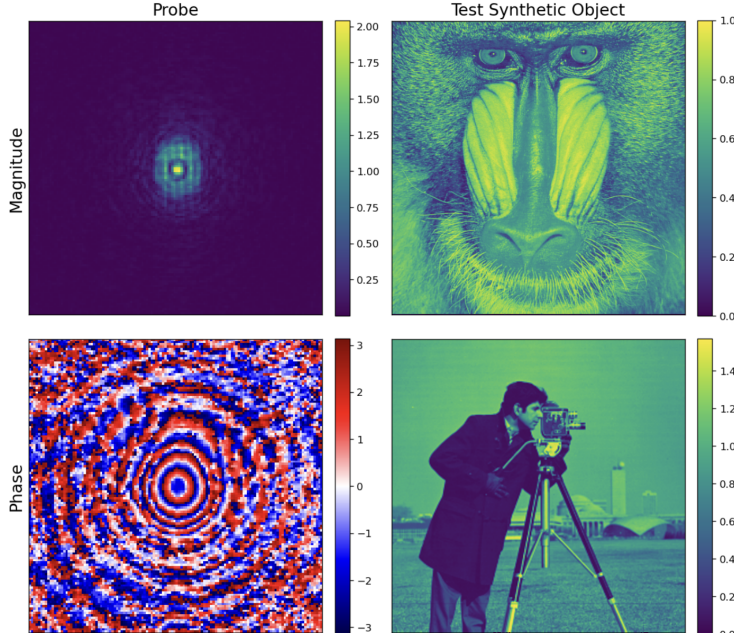


Figure 3: Columns (left to right) show the magnitude (top) and phase (bottom) of the two inputs used in our numerical experiments: (1) the simulated Fresnel zone-plate probe and (2) the test synthetic object (magnitude from the Baboon image; phase from the Cameraman image).

Noise level Given noiseless intensities $\{\tilde{\mathbf{d}}_k\}_{k=1}^N$ and noisy measurements $\{\mathbf{d}_k\}_{k=1}^N$, define the noise realizations $\mathbf{n}_k := \mathbf{d}_k - \tilde{\mathbf{d}}_k$. We report the noise level as a noise amplitude percentage based on 2 norms:

$$\text{Noise\% (amplitude)} = 100 \sqrt{\frac{\sum_{k=1}^N \|\mathbf{n}_k\|_2^2}{\sum_{k=1}^N \|\tilde{\mathbf{d}}_k\|_2^2}}.$$

Quality metrics We evaluate the reconstruction quality using two metrics: *residual* and *error*. For a reconstruction \mathbf{z} , the residual is $\Phi(\mathbf{z})$. The error is measured as the absolute ℓ^2 -norm difference between the element-wise magnitudes of the reconstruction and the ground truth object, i.e., $\|\mathbf{z} - \mathbf{z}^*\|_2$.

Stopping criterion Let $(\mathbf{Q}^{(t)}, \mathbf{z}^{(t)})$ denote the iterates at the outer iteration t , and let the residual be the exit-wave misfit (see Eqn. (1))

$$r_t := \Phi(\mathbf{Q}^{(t)}, \mathbf{z}^{(t)})$$

as in (1). We monitor the w -point moving average

$$\bar{r}_t := \frac{1}{w} \sum_{i=0}^{w-1} r_{t-i}, \quad \bar{r}_t^* := \min_{s \leq t} \bar{r}_s.$$

With $w = 5$ (window) and $p = 10$ (patience), the run terminates at the first $t \geq w$ for which

$$\bar{r}_t \geq \bar{r}_t^*$$

holds for p consecutive checks.

4.2 Overlap Ratio

We compare eMAGPIE and rPIE under three probe–object overlap ratios: 50%, 75%, and 87.5%. We set the regularization constant α according to the overlap: $\alpha = 0.05$ at 50% overlap, and $\alpha = 0.01$ at 75% and 87.5% overlap. Convergence metrics and reconstructions for all three settings are shown in Fig. 4, 5, and 6; in all cases, eMAGPIE attains lower misfits and produces higher-quality reconstructions.

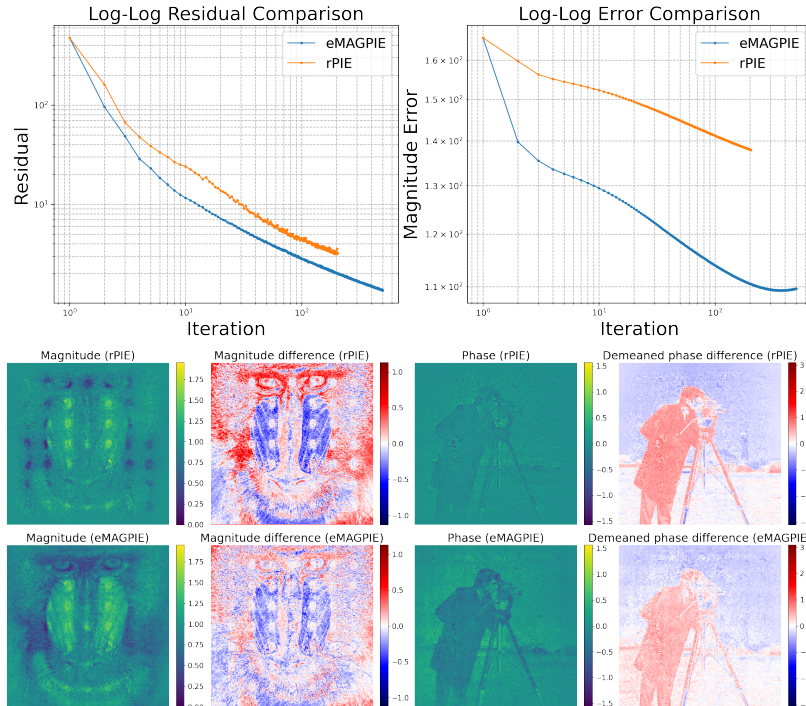


Figure 4: Synthetic data, 50% overlap. **Top:** convergence curves for rPIE and eMAGPIE showing the data misfit residual and the reconstruction error versus iteration. **Bottom:** final reconstructions for each method (magnitude and demeaned phase), together with their corresponding error maps against the ground truth. Both algorithms use the same object regularization constant $\alpha = 0.01$ and ePIE-style probe update, and early stopping based on the moving average of the last five residuals.

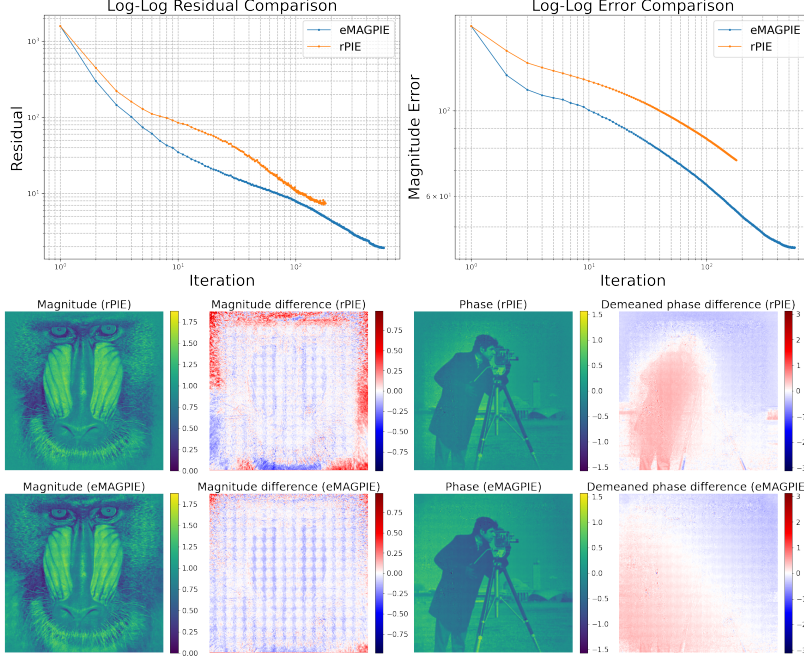


Figure 5: Synthetic data, 75% overlap. **Top:** convergence curves for rPIE and eMAGPIE showing the data misfit residual and the reconstruction error versus iteration. **Bottom:** final reconstructions for each method (magnitude and demeaned phase), together with their corresponding error maps against the ground truth. Both algorithms use the same object regularization constant $\alpha = 0.01$ and ePIE-style probe update, and early stopping based on the moving average of the last five residuals.

4.3 Robustness to Noise

To evaluate robustness against experimental noise, we compare eMAGPIE and rPIE at a fixed 75% probe–object overlap with a fixed regularization constant $\alpha = 0.05$. Noisy datasets are generated by Poisson sampling, and we test three noise levels: 5%, 10%, and 20%. In addition to the stopping criterion based on the exit-wave misfit, we impose a floor-based rule: we compute a “noise residual” by evaluating the exit-wave misfit at the ground-truth object and probe (using the true scan positions) on the noisy data, and we terminate once the running residual drops below 0.9 times this floor. Convergence and reconstruction quality for the three noise levels are shown in Fig. 7, 8, and 9; across all settings, eMAGPIE attains lower residuals and superior reconstructions compared to rPIE.

4.4 Real-data Experiment

The ptychographic scan was performed on the Velociprobe [27] at the 2-ID-D beamline of the Advanced Photon Source, Argonne National Laboratory. A 10 keV monochromatic x-ray beam was focused by a Fresnel zone plate (outermost zone width 50 nm; diameter 180 μm). A gold test sample was placed approximately 200 μm from the focal spot, yielding an illumination of about 330 nm full width at half maximum (FWHM). The sample was raster-scanned with a step size of 100 nm. Coherent diffraction patterns were recorded on a Dectris EIGER detector (pixel size 75 μm) positioned 1.95 m downstream of the sample.

From the dataset, we read the real space pixel size dx , wavelength λ , diffraction patterns $\{d_k\}$ (cropped to 256 \times 256), and the scanning coordinates (ppX, ppY) in meters. Scan positions were converted to pixel units via $(x_{\text{px}}, y_{\text{px}}) = (\text{ppX}/dx, \text{ppY}/dx)$ and then sub-sampled on a 121 \times 121 grid in two ways: every other position in each axis (resulting in 61 \times 61 = 3721 frames) and every fourth (31 \times 31 = 961 frames).

We also compare this with the current practice LSQML method [28] implemented in the PtyChi package [29].

Probe initialization. We generate $Q^{(0)}$ from a Fresnel zone plate (FZP) model. Using the wavelength λ , grid size $N=256$, sample pixel size dx , and the “velo” FZP parameters $(R_n, dR_n) = (90 \mu\text{m}, 50 \text{ nm})$ (diameter $D_{\text{FZP}} = 180 \mu\text{m}$, central stop $D_H = 60 \mu\text{m}$), we compute the focal length $f_\ell = 2R_n dR_n / \lambda$, form a circularly apertured quadratic phase at the FZP plane, and propagate to the sample by a Fresnel step over $f_\ell + L_s$ with $L_s = -3 \times 10^{-4} \text{ m}$.

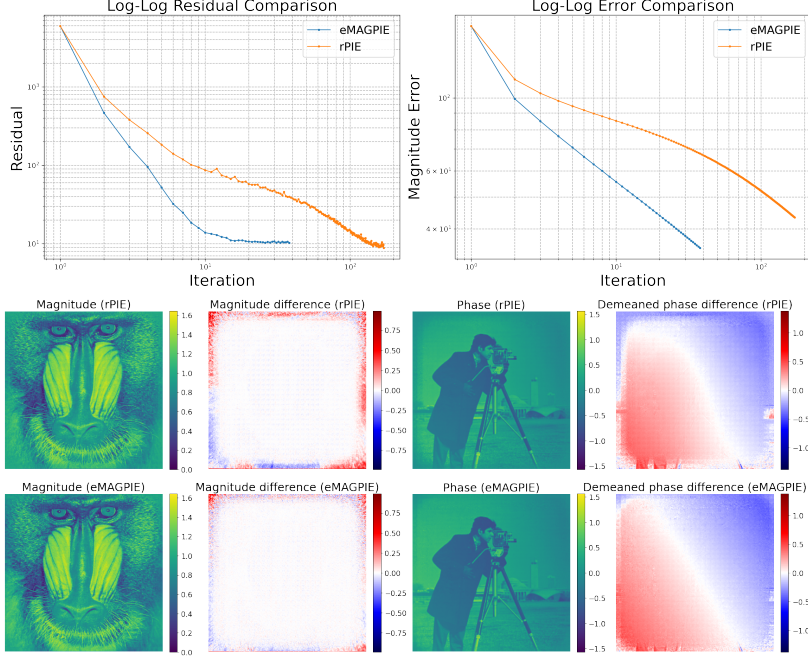


Figure 6: Synthetic data, 87.5% overlap. **Top:** convergence curves for rPIE and eMAGPIE showing the data misfit residual and the reconstruction error versus iteration. **Bottom:** final reconstructions for each method (magnitude and demeaned phase), together with their corresponding error maps against the ground truth. Both algorithms use the same object regularization constant $\alpha = 0.05$ and ePIE-style probe update, and early stopping based on the moving average of the last five residuals.

Finally, we projected $\mathbf{Q}^{(0)}$ to a fixed ℓ_2 norm using dp_avg computed from the average diffraction intensity (see Sec. 4.1), i.e., $\mathbf{Q}^{(0)} \leftarrow \mathbf{Q}^{(0)} \text{dp_avg} / \|\mathbf{Q}^{(0)}\|_2$.

Object initialization. The object was initialized to a constant field with a small random perturbation: $\mathbf{z}^{(0)} \equiv 1$ plus i.i.d. complex noise of amplitude 10^{-2} on the same grid as the suggested object field of view.

Reconstruction settings. We compared rPIE, eMAGPIE, and LSQML under identical data splits and initialization. For rPIE and eMAGPIE, we used the regularization constant $\alpha = 0.5$ and the ePIE-style probe update. For LSQML, we used the Gaussian noise model with diagonal preconditioning built from all modes. For all methods: batch size 1 (randomized scan order), fixed scan positions (no position refinement).

Phase visualization and post-processed zoom. For each reconstructed complex object $\hat{\mathbf{z}}$, we display (i) the phase and (ii) a post-processed zoom-in that removes a global phase ramp. On the cropped complex field, we form the wrapped phase image and fit a plane $ax + by + c$ (least squares) over the physical coordinate grid. Subtracting $ax + by$ removes the global linear ramp while preserving the local phase structure. The complex field is reassembled as $|\cdot| e^{i(\cdot - ax - by)}$, i.e., the magnitude remains unchanged.

Figures 10 and 11 show, for real data, the raw reconstructed phase maps (top rows) alongside the post-processed zoom-ins (bottom rows) for eMAGPIE, rPIE, and LSQML at overlap ratios of 87.6% and 93.8%, respectively. At the lower overlap (Fig. 10), eMAGPIE produces visibly smoother and more coherent phase reconstructions, with reduced ripple/stripping and cleaner backgrounds; the zoom-ins also reveal sharper features and fewer stitching artifacts compared with rPIE and LSQML, which exhibit residual phase corrugations and speckle-like noise. At the higher overlap (Fig. 11), all methods improve, and the differences narrow.

5 Conclusion

We presented a stochastic multigrid majorization–minimization framework for blind ptychographic phase retrieval. The method accelerates PIE-type schemes via a geometric-mean, phase-aligned joint object–probe update together with

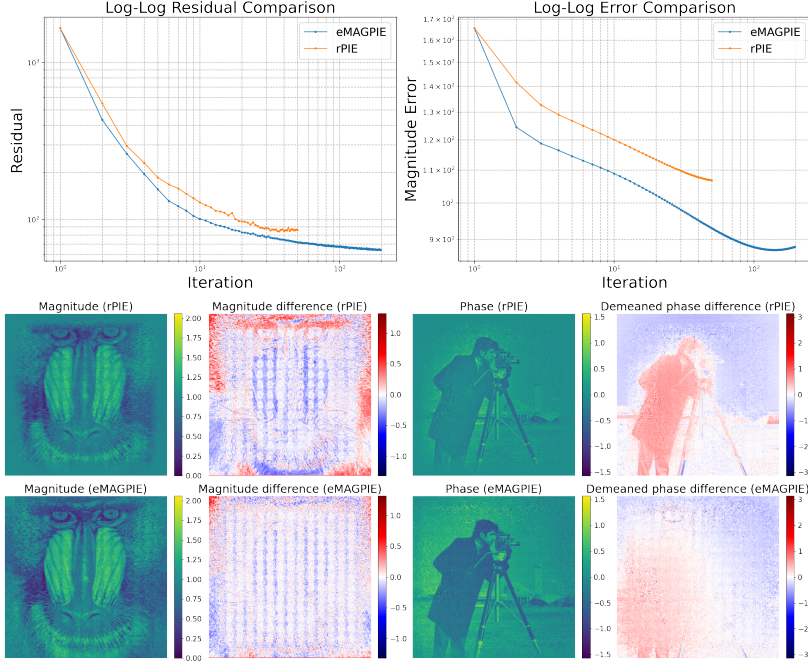


Figure 7: Top: comparison of convergence metrics; Bottom: comparison of final reconstructions. Synthetic data at 75% overlap and 5% noise (amplitude). Both eMAGPIE and rPIE use identical regularization constant $\alpha = 0.05$. Early stopping uses (i) a moving average over the last 5 residuals with patience 5, and (ii) a floor rule that terminates when the residual falls below 0.9 times the noise residual (evaluated at the ground-truth object and probe on the noisy data).

rigorously constructed coarse-grid surrogate models. It guarantees a strict decrease of the sampled surrogate at each iteration, embeds a multilevel hierarchy in which coarse-grid regularization is selected automatically by fine-coarse consistency, and preserves the standard rPIE hyperparameter set while markedly improving both convergence speed and reconstruction fidelity.

Looking ahead, we will extend the framework to minibatched updates for GPU acceleration and explore adaptive scheduling across grid levels. The multigrid-surrogate paradigm developed here is general and readily transferable to other large-scale phase-retrieval and coherent diffractive imaging problems.

6 Acknowledgments

This material was based upon work supported by the U.S. Department of Energy, Office of Science, Offices of Advanced Scientific Computing Research and Basic Energy Sciences under contract DE-AC02-06CH11357.

References

- [1] R. Hoppe, J. Reinhardt, G. Hofmann, J. Patommel, J.-D. Grunwaldt, C. D. Damsgaard, G. Wellenreuther, G. Falkenberg, and C. G. Schroer. High-resolution chemical imaging of gold nanoparticles using hard x-ray ptychography. *Applied Physics Letters*, 102(20):203104, 05 2013.
- [2] Joanne Morrison, Lotta Räty, Poppy Marriott, and Peter O'Toole. Ptychography –a label free, high-contrast imaging technique for live cells using quantitative phase information. *Scientific Reports*, 3(1):2369, 2013.
- [3] Akihiro Suzuki, Kei Shimomura, Makoto Hirose, Nicolas Burdet, and Yukio Takahashi. Dark-field x-ray ptychography: Towards high-resolution imaging of thick and unstained biological specimens. *Scientific Reports*, 6(1):35060, 2016.
- [4] Mirko Holler, Manuel Guizar-Sicairos, Esther H. R. Tsai, Roberto Dinapoli, Elisabeth Müller, Oliver Bunk, Jörg Raabe, and Gabriel Aeppli. High-resolution non-destructive three-dimensional imaging of integrated circuits. *Nature*, 543(7645):402–406, 2017.

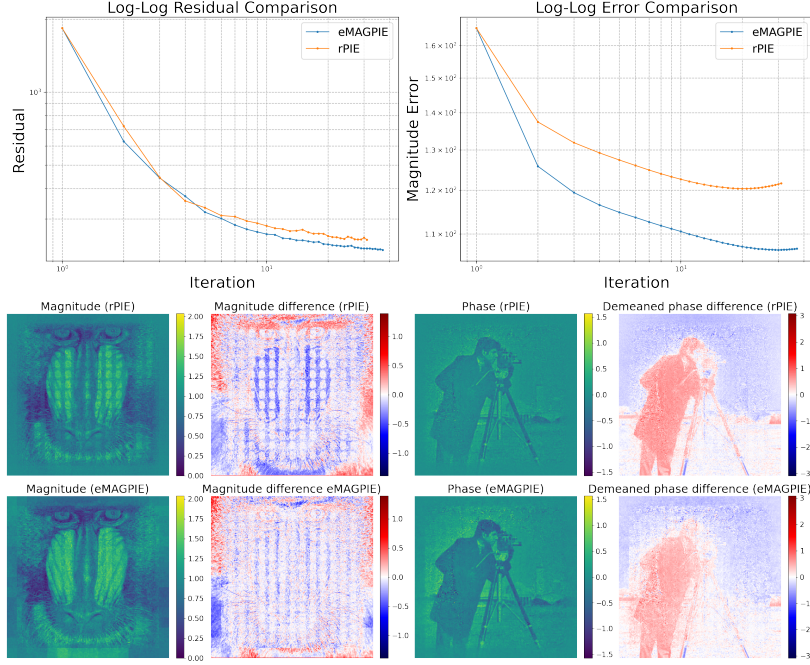


Figure 8: Top: comparison of convergence metrics; Bottom: comparison of final reconstructions. Synthetic data at 75% overlap and 10% noise (amplitude). Both eMAGPIE and rPIE use identical regularization constant $\alpha = 0.05$. Early stopping uses (i) a moving average over the last 5 residuals with patience 5, and (ii) a floor rule that terminates when the residual falls below 0.9 times the noise residual (evaluated at the ground-truth object and probe on the noisy data).

- [5] Yi Jiang, Junjing Deng, Yudong Yao, Jeffrey A. Klug, Sheikh Mashrafi, Christian Roehrig, Curt Preissner, Fabricio S. Marin, Zhonghou Cai, Barry Lai, and Stefan Vogt. Achieving high spatial resolution in a large field-of-view using lensless x-ray imaging. *Applied Physics Letters*, 119(12):124101, 09 2021.
- [6] John Rodenburg and Andrew Maiden. *Ptychography*, pages 819–904. Springer International Publishing, Cham, 2019.
- [7] J. M. Rodenburg and H. M. L. Faulkner. A phase retrieval algorithm for shifting illumination. *Applied Physics Letters*, 85(20):4795–4797, 11 2004.
- [8] Andrew M. Maiden and John M. Rodenburg. An improved ptychographical phase retrieval algorithm for diffractive imaging. *Ultramicroscopy*, 109(10):1256–1262, 2009.
- [9] Andrew Maiden, Daniel Johnson, and Peng Li. Further improvements to the ptychographical iterative engine. *Optica*, 4(7):736–745, Jul 2017.
- [10] William L. Briggs, Van Emden Henson, and Steve F. McCormick. *A Multigrid Tutorial, Second Edition*. Society for Industrial and Applied Mathematics, second edition, 2000.
- [11] Stephen G. Nash. Properties of a class of multilevel optimization algorithms for equality-constrained problems. *Optimization Methods and Software*, 29(1):137–159, 2014.
- [12] Stephen G. Nash. A multigrid approach to discretized optimization problems. *Optimization Methods and Software*, 14(1-2):99–116, 2000.
- [13] Zichao Di, Maria Emelianenko, and Stephen Nash. Truncated newton-based multigrid algorithm for centroidal voronoi diagram calculation. *Numerical Mathematics: Theory, Methods and Applications*, 5(2):242–259, 2012.
- [14] Robert Michael Lewis and Stephen G. Nash. Model problems for the multigrid optimization of systems governed by differential equations. *SIAM Journal on Scientific Computing*, 26(6):1811–1837, 2005.
- [15] Barbara Kaltenbacher. On the regularizing properties of a full multigrid method for ill-posed problems. *Inverse Problems*, 17(4):767, aug 2001.
- [16] Robert Michael Lewis and Stephen G. Nash. Model problems for the multigrid optimization of systems governed by differential equations. *SIAM Journal on Scientific Computing*, 26(6):1811–1837, 2005.

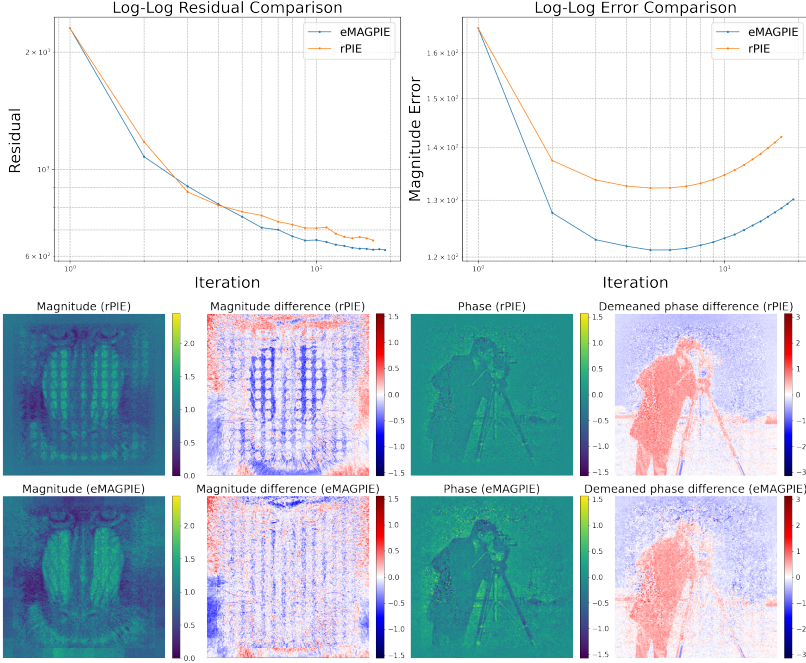


Figure 9: Top: comparison of convergence metrics; Bottom: comparison of final reconstructions. Synthetic data at 75% overlap and 20% noise (amplitude). Both eMAGPIE and rPIE use identical regularization constant $\alpha = 0.05$. Early stopping uses (i) a moving average over the last 5 residuals with patience 5, and (ii) a floor rule that terminates when the residual falls below 0.9 times the noise residual (evaluated at the ground-truth object and probe on the noisy data).

- [17] Alfio Borzì and Volker Schulz. Multigrid methods for pde optimization. *SIAM Review*, 51(2):361–395, 2009.
- [18] Samy Wu Fung and Zichao Wendy Di. Multigrid optimization for large-scale ptychographic phase retrieval. *SIAM Journal on Imaging Sciences*, 13(1):214–233, 2020.
- [19] Borong Zhang, Qin Li, and Zichao Wendy Di. Magpie: Multilevel-adaptive-guided solver for ptychographic phase retrieval, 2025.
- [20] Serge Lang. *Complex Analysis*. Graduate Texts in Mathematics. Springer New York, NY, 2 edition, June 2013.
- [21] Ken Kreutz-Delgado. The complex gradient operator and the cr-calculus, 2009.
- [22] Tianyu Qiu, Prabhu Babu, and Daniel P. Palomar. Prime: Phase retrieval via majorization-minimization technique. In *2015 49th Asilomar Conference on Signals, Systems and Computers*, pages 1681–1685, 2015.
- [23] Julien Mairal. Stochastic majorization-minimization algorithms for large-scale optimization. In C.J. Burges, L. Bottou, M. Welling, Z. Ghahramani, and K.Q. Weinberger, editors, *Advances in Neural Information Processing Systems*, volume 26. Curran Associates, Inc., 2013.
- [24] Hanbaek Lyu. Stochastic regularized majorization-minimization with weakly convex and multi-convex surrogates. *Journal of Machine Learning Research*, 25(306):1–83, 2024.
- [25] Julien Mairal. Incremental majorization-minimization optimization with application to large-scale machine learning. *SIAM Journal on Optimization*, 25(2):829–855, 2015.
- [26] J.M. Rodenburg. Ptychography and related diffractive imaging methods. volume 150 of *Advances in Imaging and Electron Physics*, pages 87–184. Elsevier, 2008.
- [27] Junjing Deng, Curt Preissner, Jeffrey A. Klug, Sheikh Mashrafi, Christian Roehrig, Yi Jiang, Yudong Yao, Michael Wojcik, Max D. Wyman, David Vine, Ke Yue, Si Chen, Tim Mooney, Maoyu Wang, Zhenxing Feng, Dafei Jin, Zhonghou Cai, Barry Lai, and Stefan Vogt. The velociprobe: An ultrafast hard x-ray nanoprobe for high-resolution ptychographic imaging. *Review of Scientific Instruments*, 90(8):083701, 08 2019.
- [28] Michal Odstrčil, Andreas Menzel, and Manuel Guizar-Sicairos. Iterative least-squares solver for generalized maximum-likelihood ptychography. *Opt. Express*, 26(3):3108–3123, Feb 2018.

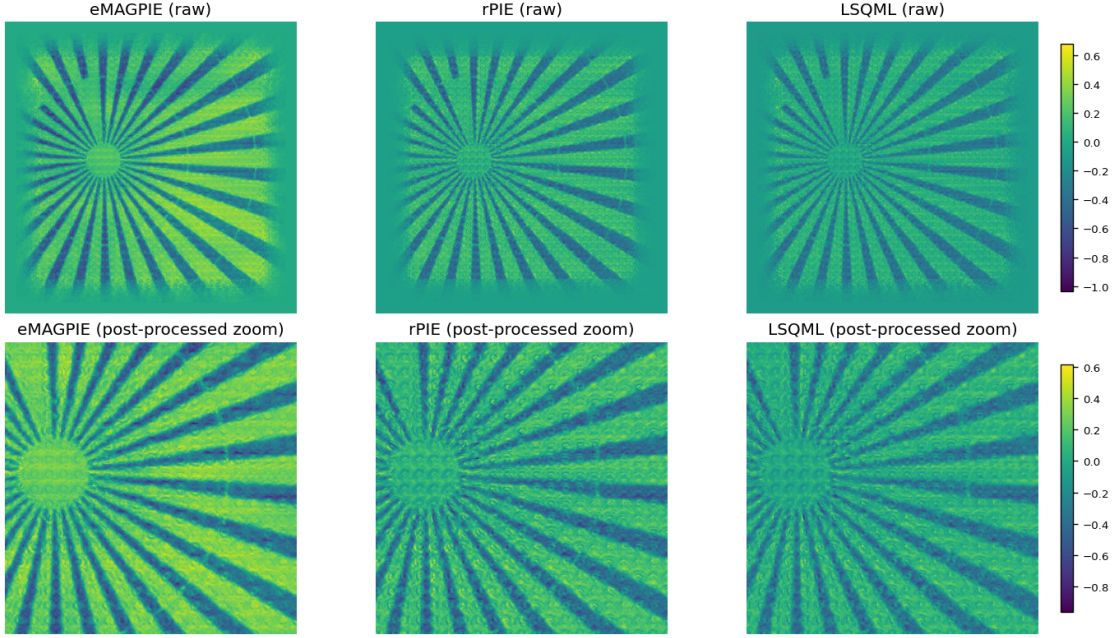


Figure 10: Unprocessed phases (top) and post-processed zoom-ins (bottom) for eMAGPIE, rPIE, and LSQML.

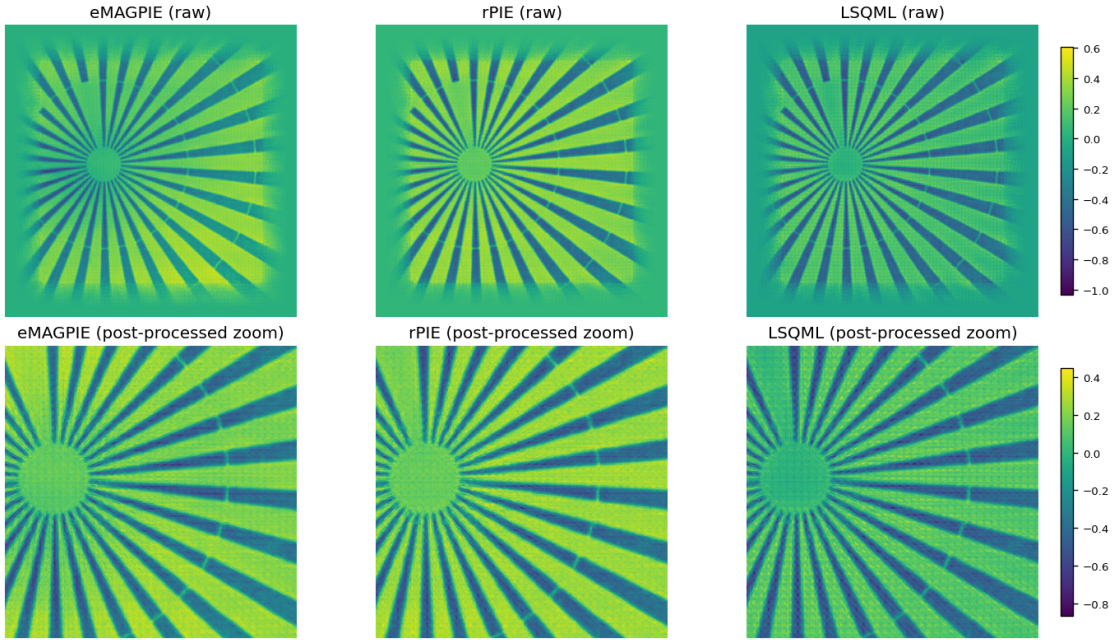


Figure 11: Unprocessed phases (top) and post-processed zoom-ins (bottom) for eMAGPIE, rPIE, and LSQML.

[29] Ming Du, Hanna Ruth, Steven Henke, Yi Jiang, Viktor Nikitin, Ashish Tripathi, Junjing Deng, Jeffrey Klug, Peco Myint, Tao Zhou, Nicholas Schwarz, Mathew Cherukara, Alec Sandy, and Stefan Vogt. Pty-chi: A pytorch-based modern ptychographic data analysis package, 2025.